PNAS RESEARCH ARTICLE | EARTH, ATMOSPHERIC, AND PLANETARY SCIENCES OPEN ACCESS

Modeling the dynamics of aeolian meter-scale bedforms induced by bed heterogeneities

Camille Rambert[a,1], Joanna M. Nield[b], Clément Narteau[c], Pauline Delorme[d], Giles F. S. Wiggs[e], Matthew C. Baddock[f], Jim Best[g], Kenneth T. Christensen[h], and Philippe Claudin[a,1]

Affiliations are included on p. 9.

Edited by Michael Manga, University of California, Berkeley, CA; received December 15, 2024; accepted April 4, 2025

Desert surfaces are typically nonuniform, with individual sand dunes generally surrounded by gravel or nonerodible beds. Similarly, beaches vary in composition and moisture that enhances cohesion between the grains. These bed heterogeneities affect the aeolian transport properties greatly and can then influence the emergence and dynamics of bedforms. Here, we propose a model that describes how, due to transport capacity being greater on consolidated than erodible beds, patches of sand can grow, migrate, and spread to form bedforms with meter-scale length. Our approach has a quantitative agreement with high-resolution spatiotemporal observations, where conventional theory would predict the disappearance of these small bedforms. A crucial component of the model is that the transport capacity does not instantly change from one bed configuration to another. Instead, transport capacity develops over a certain distance, which thereby determines the short-term evolution of the bedform. The model predicts various stages in the development of these meter-scale bedforms, and explains how the evolution of bed elevation profiles observed in the field depends on the duration of the wind event and the intensity of the incoming sand flux. Our study thus sheds light on the initiation and dynamics of early-stage bedforms by establishing links between surface properties, emerging sand patterns, and protodunes, commonly observed in coastal and desert landscapes.

sediment transport | heterogeneous beds | ephemeral bedforms | dune emergence

Significance

We present a model to explain the emergence of meter-scale bedforms that grow in coarse-grained interdune areas or on moist beaches. We show that the existing theory of dune dynamics must be extended to account for the spatial variation of wind transport capacity over bed heterogeneities, with enhanced transport over consolidated rather than erodible surfaces. The quantitative agreement between the model predictions and a unique set of high-precision field data acquired in the Namib Desert allows us to theoretically explore the different dynamics of such emerging bedforms, which can eventually disappear or lead to dune formation. This work provides ways to interpret the initiation and evolution of small bedforms, and facilitates the estimation of aeolian transport in diverse environments.

Aeolian dunes are often sufficiently large to accommodate seasonal variations of surface winds, resulting in a diversity of shapes, orientations, and dynamics according to sand availability and environmental conditions (1). At the same time, smaller bedforms, either ephemeral or destined to grow into protodunes (2, 3), can emerge during short individual wind events (4–8). Such early stage bedforms are important to study as they reveal some of the key processes of dune dynamics at work before they become affected by more complicated phenomena such as coarsening and nonlinear effects (9). Although some of these emerging bedforms have been clearly identified as resulting from the unstable nature of a flat sand bed with a length selected by the interplay between topography, wind flow, and sediment transport (10–12), others, with sizes typically smaller than the cut-off length ($\simeq$10 m) below which dunes are not expected to grow, exhibit their own morphodynamics (13). This is particularly the case for small, meter-scale, sandy bedforms that develop over more consolidated beds. They have been associated with sediment transport properties that vary due to spatial heterogeneities of the substrate, including transitions between consolidated and erodible beds (14). These bedforms are distinct from decimeter-scale wind ripples, which adorn the flanks of dunes and sandy surfaces in general, and whose dynamics is due to the properties of saltating particles when they impact a fully erodible granular bed (15–19). The manner in which such meter-scale bedforms may, or may not, grow into protodunes and dunes has yet to be investigated precisely, and this is one of the purposes of the present work.

Since the pioneering studies of Bagnold on the physics of wind-blown sand (20, 21), the properties of aeolian saltation and, in particular, the quantification of the grain trajectories and transport capacity of a wind of a given strength have been investigated (22–30) and reviewed (31, 32). Saltation has also been shown to be sensitive to the nature of the bed over which the grains rebound, with enhanced transport over a consolidated surface (either solid, gravel, or moist/cohesive) in comparison to that on an erodible sandy layer (33–35). Rebounds are less dissipative over a rigid surface than a granular one, resulting in higher saltation layers (33). This has consequences for the feedback that moving grains exert on the wind flow. For ordinary saltation on sand beds, the transport

Author contributions: C.R., J.M.N., C.N., P.D., G.F.S.W., M.C.B., J.B., K.T.C., and P.C. designed research; C.R., J.M.N., C.N., P.D., G.F.S.W., M.C.B., and P.C. performed research; C.R., C.N., and P.C. contributed new reagents/analytic tools; C.R., J.M.N., C.N., and P.C. analyzed data; and C.R., J.M.N., C.N., P.D., G.F.S.W., M.C.B., J.B., K.T.C., and P.C. wrote the paper.

The authors declare no competing interest.

This article is a PNAS Direct Submission.

[1]To whom correspondence may be addressed. Email: camille.rambert@espci.fr or philippe.claudin@espci.fr.

This article contains supporting information online at https://www.pnas.org/lookup/suppl/doi:10.1073/pnas.2426143122/-/DCSupplemental.

Published May 16, 2025.

layer of almost constant height (Bagnold's focal height) accommodates saltating grains at a large enough volume fraction to reduce the basal wind shear velocity to its transport threshold value (31, 36). The velocity of the moving grains is thus constant, independent of wind speed (37). By contrast, over consolidated beds, the grains, which move in a more expanded transport layer, have a weaker and more dilute feedback on the flow, so that their velocity typically follows that of the wind. This explains a ratio in transport capacities between consolidated and erodible beds that scales with the wind shear velocity (33, 38, 39).

As proposed by refs. 14 and 40, reduction in sediment transport capacity where the bed transitions from consolidated to erodible is a way to amplify local sand deposition and trigger the development of small bedforms. The aim herein is to investigate more precisely by which processes, and at which scales, the growth and propagation of early-stage bedforms can occur. This also raises the question as to how the standard dune model, which predicts steady propagative flat domes at a size close to the cut-off length—but not smaller—almost independently of the incoming sand flux (41), can be generalized to describe these meter-scale growing bedforms, which are sensitive to sand supply. Here, we use field measurements of the evolution of small bedforms in the Namib Desert with a high spatial precision (0.01 m) and over a short time period ($\simeq$1 h). We test and develop components of a dune model in order to generalize the analysis of aeolian bedforms over a previously inaccessible range of length scales and through transient dynamics that have not yet been explored.

The paper starts with the description of the field location and data acquisition. We then present the model, highlighting its additional components with respect to the reference dune emergence theory, especially a length scale that quantifies the distance over which the consolidated/erodible bed transition occurs. Depending on the parameter values, in particular the input sand flux and this length scale, different dynamics are found, by which an initially flat patch after a certain time either disappears, grows while migrating, or spreads both up and downwind. The fit of these parameters to reproduce quantitatively the spatiotemporal variations of the bedform profile measured in the field gives good confidence on the relevance of these processes associated with bed heterogeneities. Understanding of the microscopic nature of this transition length scale is, however, an essential question that remains to be investigated further. These results also open discussion on the longer-term evolution of such out-of-equilibrium bedforms, which can quickly appear, grow, and/or disappear, and motivate future studies on their interactions and dynamics.

Meter-Scale Sand Bedforms in the Namib Desert

Field measurements were collected of sandy bedforms migrating over a gravel surface at Helga's Interdune, Gobabeb, Namibia (Fig. 1*A*). This location has a wide interdune surrounded by linear dunes to the east and west, and a crossing dune to the south. Measurements of growing and migrating bedforms were undertaken during an easterly wind on the 13th September 2022 (42), while measurements of shrinking bedforms were undertaken during an easterly wind on the 12th September 2023 (43). Grain size distributions from samples collected on these large dunes, as well as in traps located next to the small bedforms, support the hypothesis that the sand feeding these bedforms comes from the dunes (*SI Appendix*, Fig. S18). Surface topography was measured using a Leica P20 and P50 Scanstation for 2022 and 2023 datasets respectively, measuring at a horizontal resolution of 3.1 mm at 10 m. During both measurement periods, bedforms from within a larger field of similar forms (Fig. 1*A*) were chosen for further analysis because they were close to the Terrestrial Laser Scanner (TLS) and with its sight line perpendicular to the wind direction, in order to minimize occlusion of the underlying surface by the saltation cloud. Near-surface wind speed and direction within the bedform field were recorded on the consolidated bed at a height of 0.24 m and frequency of 10 Hz using a Campbell CSAT 3D sonic anemometer located $\simeq$50 m away from the bedform.

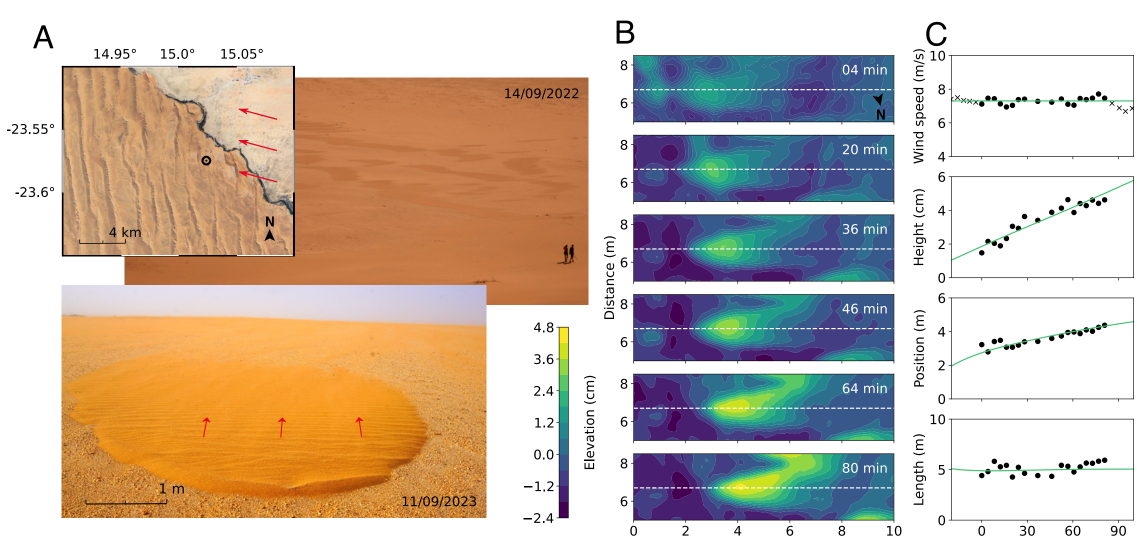

Fig. 1. Morphodynamics of meter-scale sand bedforms at the northern border of the Namib Sand Sea, Namibia. (*A*) Location of the site close to Gobabeb Namib Research Institute (15°01′31″E and 23°34′31′S). *Top* photo: Aerial view of the site. *Middle* photo: View of the field of bedforms. *Bottom* photo: closer view of an individual bedform. Red arrows show wind direction. (*B*) Elevation maps of a growing and migrating bedform measured over 80 min (color bar on the *Left*). The measurements began at 9:40 am on the 13th September 2022. (*C*) Variation over time of the bedform height, position, and length (three *Lower* panels), as measured along the central longitudinal transect (dashed line in *B*). Solid lines are obtained using the model with best fit parameters to the data: $\{L_0/L_{sat}, q_{in}/q^e_{sat}\} = \{2.0, 2.0\}$; see also Fig. 4. During the measurement period, the wind was very consistent in strength (*Top* panel) and direction (75° anticlockwise from North; see *SI Appendix*, Fig. S14).

Each TLS scan was filtered for saltating grains using a radial filter (35° angle) and subsequently identified surface points were gridded at 0.01 m resolution using the methods described in ref. 34. Underlying topography was detrended for slope by fitting a surface through points where the surface change between all scans was less than 2.0×10^{-4} m. This methodology gives a resolution of 5.5×10^{-4} m for vertical change and a horizontal resolution of 0.01 m (13). The detrended surface was also smoothed using a 0.45×0.45 m^2 mean moving window filter to remove ripples (13). These detrending and smoothing data processes are illustrated in *SI Appendix*, Fig. S17. Profiles $h(x)$ were then extracted from the centerline of individual bedform Digital Elevation Models (DEM) at successive times (Fig. 1*B*).

For each of these profiles, the height H and position of the crest of the bedform can be deduced by fitting a parabola around the maximum of the elevation. Similarly, the upwind and downwind edges of the bedform can be determined, but this is a less precise measurement because of data noise where the elevation is small. A more robust method to estimate bedform length is to compute the area $\Delta = \int h(x)\mathrm{d}x$ between these two edges and define the length as $2\Delta/H$. The advantage here is that this triangle-like definition is less sensitive to the precise location of these edges, as the corresponding side regions do not contribute substantially to the integral. Note that, when dealing with theoretical profiles only, i.e. not related to data analysis or fitting, the ordinary definition of bedform length (difference between edge positions) is used instead.

For the bedform whose DEM evolution is displayed in Fig. 1*B*, we thus obtain its height, position, and length as a function of time, showing a clear growth and migration, while its length remains fairly constant over the observation duration (Fig. 1*C*). These are the data against which the performance of our model (described below) is tested.

A Model for the Dynamics of Meter-Scale Sand Bedforms

The model proposed herein for reproducing the dynamics of meter-scale sand bedforms is based on the core of well-established dune continuum approaches (41, 44–50). First, we present the general form of the governing equations that relate the bed elevation profile h, saltation flux q, and bed shear stress τ. We then introduce two additional key components to account for the difference in transport capacity between erodible and consolidated beds (14, 33, 51). These are distinct maximum transport rates and, most importantly, a new length scale, L_0, which governs changes in transport capacity following shifts in surface properties on heterogeneous beds. For the sake of simplicity, the model is assumed to be homogeneous in the direction transverse to the wind, and we consider only the horizontal wind direction x and the vertical axis of the bed elevation profile. This will be relevant for the dynamics over time t of the central transect of the bedform, which we assume to be representative of the entire object.

Governing Equations of Dune Theory. The first equation is mass conservation, which stipulates that the erosion/deposition rate must balance the spatial variations in sediment flux:

$$\partial_t h + \partial_x q = 0. \qquad [1]$$

q is here defined as a volumetric flux: It counts the volume of the grains passing through a vertical surface of unit transverse width per unit time. This volume is taken at the bed packing fraction, thus eliminating any additional factors in Eq. **1**, also referred to as the Exner equation (52, 53). As we consider a finite amount of sand deposited on a consolidated bed, the variations in flux must account for the fact that no erosion occurs below the reference level $h = 0$ (*Materials and Methods*).

The second component of the model differentiates between the flux q and the transport capacity, or saturated sand flux, q_{sat}. These two quantities coincide in the steady state case of a homogeneous flat bed but are generally distinct. Here, we assume that q tends to q_{sat} following a first-order relaxation process:

$$L_{\mathrm{sat}}\partial_x q = q_{\mathrm{sat}} - q. \qquad [2]$$

This equation involves a key spatial scale, the saturation length L_{sat}, which encodes the typical lag by which q is delayed with respect to q_{sat} (6, 12, 36, 41, 49, 50, 54–58). Because of the nonerodible reference level $h = 0$, this equation cannot be satisfied if it would lead to erosion of the consolidated bed. To illustrate this point, consider the simple situation where saltation occurs over a perfectly flat consolidated bed at a transport rate q that is below its transport capacity q_{sat}. In this case, Eq. **1** would predict erosion. However, to keep q constant, we impose $\partial_x q = 0$, thereby ensuring that the bed elevation remains at $h = 0$.

To account for changes in transport capacity, q_{sat} is an increasing function of the bed shear stress, τ, which itself is modified by the topography. In the limit of flat bedforms, as those considered here, the relationship between the stress perturbation and h is better expressed in the Fourier space where all functions are decomposed over wavelength λ or wavenumber $k = 2\pi/\lambda$ ($\hat{f}$ will denote the Fourier transform of f). It reads

$$\hat{\tau} = \tau_0(\mathcal{A} + i\mathcal{B})k\hat{h}, \qquad [3]$$

where $\tau_0 = \rho_{\mathrm{air}} u_*^2$ is the reference stress over the flat bed, ρ_{air} is the air density, and u_* is the wind shear velocity. The two dimensionless coefficients $\mathcal{A}$ and $\mathcal{B}$ represent respectively the in-phase and in-quadrature responses of the shear stress to the bed modulation. Their values generally depend on k, but they can be taken as constants for turbulent flows over rough surfaces, which is the relevant limit for terrestrial winds over sand beds on which saltation occurs (1, 49). Here, we will take $\mathcal{A} = 3$ and $\mathcal{B} = 1.5$ as representative values of the measurements taken in the field (12, 59).

Transport Capacity on Erodible and Consolidated Beds. The transport law, i.e. the transport capacity in homogeneous and steady conditions, that relates the saturated flux to the wind shear stress depends strongly on the nature of the bed. In the reference case of saltation occurring on an erodible sandy surface, q_{sat} typically increases linearly with τ above a threshold τ_{th} (23, 31, 36, 60, 61). Here, we write it as

$$q^{\mathrm{e}}_{\mathrm{sat}}(\tau) = Q(\frac{\tau}{\tau_{\mathrm{th}}} - 1), \qquad [4]$$

where Q is a dimensional constant (in m^2 s^{-1}), which accounts for dependencies of the sand flux on environmental parameters (grain size d and density ρ_{sed}, air density ρ_{air}, gravitational acceleration g). All the values of these parameters are set below in order to compare the predictions of the model to the field data. As for the general theoretical analysis of the model, however, the results are displayed with lengths in units of L_{sat} and time in units of L^2_{sat}/Q.

The linear relationship between transport capacity q_{sat}, and bed shear stress, τ, observed in steady-state conditions can be attributed to the fact that the majority of the moving grains contributing to the flux remain close to the surface, below Bagnold's focal height. As a result of the feedback of these grains on the airflow, as well as the rebound condition on a sandy bed, their velocity is independent of the wind shear stress and equal to the transport threshold (27, 31, 36, 61). For significantly large winds, typically above a Shields number $\Theta = \tau/(\rho_{\mathrm{sed}} g d) \simeq 0.3$, a quadratic correction to this linear behavior has been proposed, associated with binary particle collisions (32, 62). Here, our field data are well below ($\Theta \simeq 0.05$) and we can thus safely neglect this correction. On the other hand, when saltation occurs over a consolidated surface, the rebounds of the grains on the bed are less dissipative and the transport layer is substantially thicker, with a vanishing feedback of moving grains on the flow. Their velocity then scales with that of the flow, i.e. $\sim\sqrt{\tau/\rho}$, which gives then an extra factor in the saturated flux (33). Here, we thus write this second transport law as

$$q^{\mathrm{c}}_{\mathrm{sat}}(\tau) = Q_{\mathrm{c}}\sqrt{\frac{\tau}{\tau_{\mathrm{th}}}}\left(\frac{\tau}{\tau_{\mathrm{th}}} - 1\right), \qquad [5]$$

where we keep the same threshold shear stress τ_{th} as in Eq. **4**. This is a good approximation and well supported by the few data available for comparison of the two transport laws (14, 33, 63). In contrast, determination of the ratio Q_{c}/Q from these data is less straightforward as it is found to vary from 1 to 3 depending on the conditions and measurement set-up. For the sake of simplicity, we set here $Q_{\mathrm{c}} = Q$, but bear in mind that this ratio is, in principle, an additional adjustable parameter of the model.

In fact, the precise parametric choices for these two transport laws do not change the results qualitatively, as long as the transport capacity is enhanced over a consolidated bed, as compared to an erodible granular surface. Much more critical, however, is the necessity to account for the transition from one law to the other, in order to reproduce the observed growth and migration of these small bedforms. This process is associated with a length scale, here denoted by L_0, that controls the change in transport capacity after a shift in bed surface properties. Such a nonabrupt transition is consistent with the observations of spatial variations of saltation over sand patches (7, 14). In the present work, L_0 is an empirical parameter, which is adjusted based on the measurements made in the field. Its dependence on grain/flow properties is part of the discussion but is clearly beyond the scope of this paper and would require further dedicated studies at the microscopic scale. In the present analysis, we simply assume that the transport capacity undergoes a linear downwind transition when the bed switches from state 1 to state 2 (consolidated to erodible or vice versa) at location x_s:

$$q_{\mathrm{sat}} = \begin{cases} q_{\mathrm{sat}_1} & \text{if } x \le x_s, \\ q_{\mathrm{sat}_1} + \dfrac{x - x_s}{L_0}(q_{\mathrm{sat}_2} - q_{\mathrm{sat}_1}) & \text{if } x_s \le x \le x_s + L_0, \\ q_{\mathrm{sat}_2} & \text{if } x \ge x_s + L_0. \end{cases} \qquad [6]$$

These expressions assume that the bed is in state 2 for more than L_0, otherwise the transition is shortened and the switch back to state 1 starts before reaching $q_{\mathrm{sat},2}$ (*SI Appendix*). One could argue that windward (from consolidated to erodible beds) and leeward (from erodible to consolidated beds) transition lengths should be different, but we have not explored this more refined option that requires an additional parameter. Several other options than the piece-wise linear form Eq. **6** have also been tested, including a smoother transition shape with a hyperbolic tangent, and a centered scheme with q_{sat} starting/ending its transition at $x_s \mp L_0/2$. Furthermore, the precise point at which the bed transitions from consolidated to erodible or vice versa is not readily discernible. Numerical simulations have demonstrated that a gradual shift from consolidated to erodible states occurs when the surface is covered by a few grains of erodible sand (63). Here, we set the switching criterion at a finite bed elevation $h_{\mathrm{s}} = 2 \times 10^{-4}\ L_{\mathrm{sat}}$, typically corresponding to 1 or 2 grain diameters. These arbitrary choices made for the shape of the transition in transport capacity and the threshold bed thickness do not qualitatively modify the results presented below, but slightly affect the position and shape of the upwind and downwind edges of the bedform.

Three Different Dynamics of Bedforms Evolution

We integrate the above equations numerically to simulate the time evolution of a bedform, starting from an almost flat patch of height H_i and limited length L_i. We find that the bedform profile does not converge toward a propagative steady state, but displays three different dynamic regimes depending on the values of the input flux q_{in} and the transition length L_0: disappearance, growth and migration, and spreading. In practice, we have used the initial profile $h(x, t = 0) = H_i\,(1 - \cos(\pi x/L_i))^{\alpha}$ for $0 \le x \le L_i$ and $h = 0$ otherwise, where the exponent was chosen large enough ($\alpha = 40$) to make the shape of this profile very flat. We have tested other profiles, like a Fermi–Dirac shape, with little difference in the results. Unless otherwise stated, we have set the initial height to $H_i = 5\,h_{\mathrm{s}}$ and length to $L_i = 5\,L_{\mathrm{sat}}$.

Growth, Migration, and Spreading. In order to illustrate and elucidate these three dynamic regimes and their associated mass balances, Fig. 2 displays the different longitudinal elevation profiles together with the flux and erosion rates. We first consider the most interesting case where the incoming flux lies between the transport capacities on consolidated and erodible beds: $q^{\mathrm{c}}_{\mathrm{sat}} > q_{\mathrm{in}} > q^{\mathrm{e}}_{\mathrm{sat}}$. The more ordinary case where q_{in} is smaller than $q^{\mathrm{e}}_{\mathrm{sat}}$ is discussed briefly at the end of this section.

The generic picture is as follows. When saltating grains move from a consolidated surface to an almost flat, sandy bedform, the transport capacity decreases from $q^{\mathrm{c}}_{\mathrm{sat}}$ to $q^{\mathrm{e}}_{\mathrm{sat}}$ over the length L_0 (Eq. **6**), but the actual sand flux q first increases. This is associated with erosion of the upwind edge of the bedform (Eq. **1**). The flux then decreases and sediment is deposited over the sand bed. It can also deposit beyond the downwind edge of the sandy area, where the output flux q_{out} is eventually released. Once again, this occurs because the switch toward the larger transport capacity on the consolidated bed is not immediate. Rather, the transport capacity increases gradually over the scale L_0. These processes of erosion and deposition on the windward and leeward margins induce a systematic migration of the bedform.

These dynamics can be investigated in more detail according to the value of q_{in}. Slightly increasing the incoming flux above $q^{\mathrm{e}}_{\mathrm{sat}}$, we first have $q_{\mathrm{out}} > q_{\mathrm{in}}$, i.e. a negative mass balance for the bedform. Its upwind side becomes steeper, but it gradually shrinks and accelerates. It eventually disappears, retaining its asymmetrical shape (Fig. 2 *A* and *B*). Increasing q_{in} further, the same asymmetry develops over a shorter time, but at

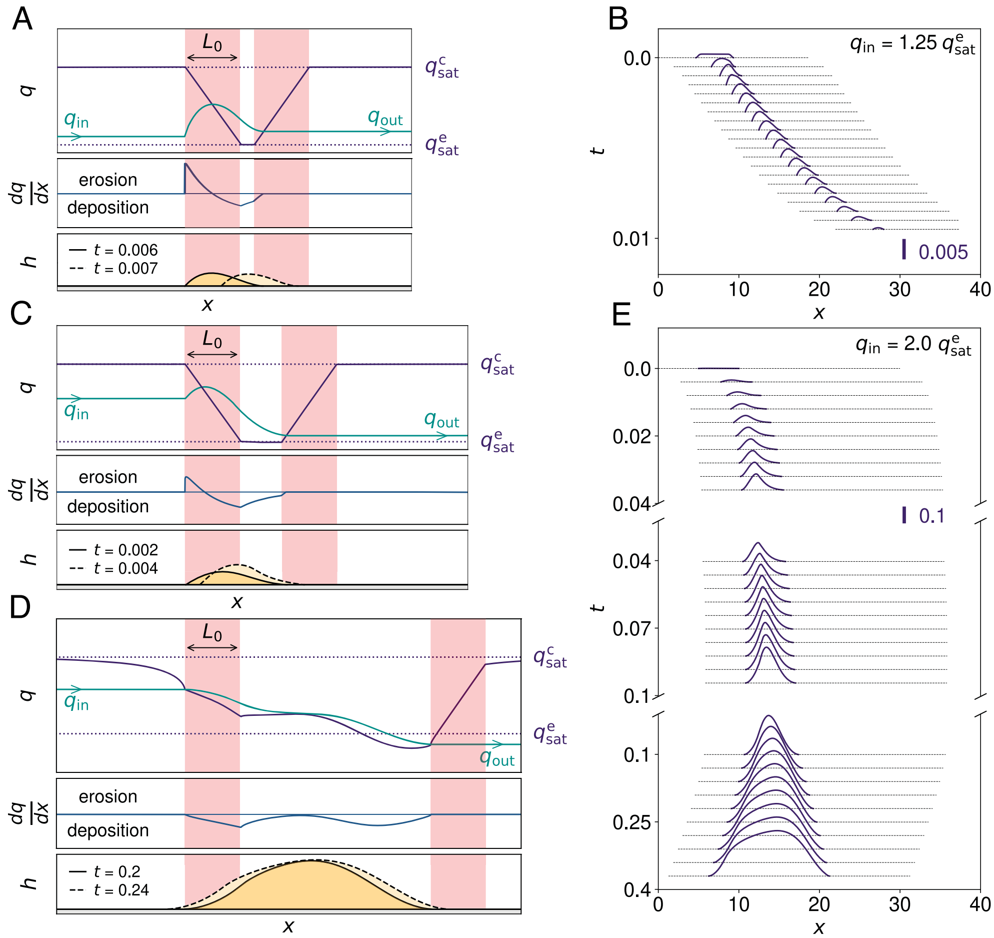

Fig. 2. Three differing dynamical regimes of the bedforms as predicted by the model. In the *Left* column, various profiles are schematized: elevation h (black), saturated q_{sat} (violet), and actual q (green) fluxes, and erosion rate dq/dx (blue). Solid and dashed black lines correspond to h at two successive times (legend), but the flux profiles are represented at the first time only. Transition zones of the transport capacity, of size L_0, are highlighted in pink. Right column: corresponding spatiotemporal diagrams of h (reference amplitude bar in *Inset*) are displayed for a given value of the input flux q_{in} (legend); see also *SI Appendix*, Fig. S2. All lengths in units of L_{sat} and times in units of L_{sat}^2/Q. For all these simulations, the model parameters are $L_0 = 2$, $L_i = 5$, and $H_i = 10^{-3}$. (*A* and *B*) Disappearing bedforms. For low values of q_{in}, the sharp increase in the sand flux on the upwind part of the patch is not compensated for by the downwind sand flux relaxation which results in $q_{out} > q_{in}$. (*C*) Growing and migrating bedforms. For larger q_{in}, the sand flux has more space to relax to a value closer to q_{sat}^{e}, resulting in $q_{out} < q_{in}$. (*D*) Spreading bedforms. The bedform eventually stops migrating and continues to grow both upwind and downwind. This last regime occurs when the shape is steep enough to significantly affect the wind flow and lower the shear stress (and thus q_{sat}) on its upwind side. See also *SI Appendix*, Fig. S1. (*E*) The spreading phase follows the migration phase as the bedform grows, and its stoss side becomes steeper.

some large enough value, the mass balance becomes positive: $q_{out} < q_{in}$. The bedform then grows and slows down as it continues to migrate (Fig. 2 *C* and *E* for $t < 0.04\ L_{sat}^2/Q$). This growth occurs mainly in height, as the length of the bedform remains fairly constant. When this growth is sustained for a sufficient time, the bedform becomes steep enough to interact significantly with the wind flow (Eq. **3**). This reduces the bed shear stress around both the windward and leeward margins (*SI Appendix*, Fig. S1), so that sand deposition occurs upwind and downwind of the bedform (*SI Appendix*, Fig. S2). As a result, its length increases, its height saturates, and a spreading dynamics follows the growth and migration regime (Fig. 2 *D* and *E* for $t > 0.1\ L_{sat}^2/Q$).

The whole sequence displayed in Fig. 2*E* runs faster for larger values of q_{in}. Furthermore, because the erosion and deposition zones result from the competition between the space variations of q_{sat} due to L_0 and the relaxation of q associated with L_{sat} (Eq. **2**), the ratio of these two length scales also governs the occurrence of the different regimes (*SI Appendix*, Figs. S3–S5).

Conditions for the Three Regimes. Fig. 3 summarizes the dominant dynamics in the different regions of the parameter space $\{q_{in}/q_{sat}^{e}, L_0\}$, after a given time $T = 0.02\ L_{sat}^2/Q$, always starting from the same initial condition. The disappearing regime is for low values of the input flux, with a systematic but rather moderate dependence on L_0. By contrast, the spreading regime concerns larger values of the input flux and its delimitation in this diagram shows a strong variation with respect to q_{in} at small L_0. In between, for moderate values of both q_{in} and L_0, growth and migration occur systematically. Not surprisingly, as discussed in the next section, this is where the majority of the field observations lie.

Fig. 3 is a generic diagram in the sense that it always shows the same organization of the different regimes, regardless of the other parameters of the model and the initial conditions. However, the exact location at which the transition occurs from one regime to another (white and black lines in Fig. 3) is somewhat sensitive to the initial length and height of the patch (*SI Appendix*, Fig. S6). It also depends on the total integration time T, especially when

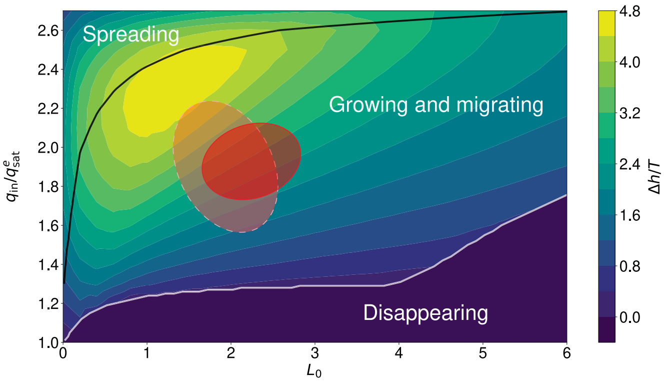

Fig. 3. Diagrammatic representation of the three dynamical regimes in the parameter space $\{q_{in}/q^e_{sat}, L_0\}$ at a given time T. The color code indicates the average growth rate of a bedform at time $T = 0.02$, starting from a flat patch $t = 0$ ($L_i = 5$, $H_i = 10^{-3}$). Black line: limit between migrating (*Below*) and spreading (*Above*) bedforms. White line: limit between growing (*Above*) and disappearing (*Below*) bedforms. The red (plain outline) and pink (dashed outline) areas show the estimated values (and their uncertainties) of input flux and transition length when the model is compared to the field data; see respectively fits in Fig. 4 (case corresponding to the red ellipse) and *SI Appendix*, Fig. S12 (pink ellipse). As can be seen in these figures, the time interval during which the growth and migration of the bedform was compared to the model was respectively 0.004 to 0.013 (Fig. 4) and 0.006 to 0.012 (*SI Appendix*, Fig. S12) in dimensionless units, hence the choice of $T = 0.02$ for this diagram, as a relevant capping rounded number.

the bedforms evolve from the growing and migrating regime to the spreading regime (Fig. 2*E*). In this case, the transition curves between these two regimes correspond to smaller values of q_{in} for larger values of T. Here, for Fig. 3, the choice of $T = 0.02$ is justified by the fact that the fitted data, which we represent with the red and pink ellipses, correspond to a growth and migration of the bedforms between 0.004 and 0.015 in dimensionless units (see next section).

To clarify the role of the initial conditions in the development of the bedform, it is interesting to consider a perfectly flat ($H_i = 0$) erodible surface of length L_i, for which an analytical solution of the model exists (*SI Appendix*). One can in particular compute, in the parametric plane $\{q_{in}, L_i\}$, the line separating the two regions where patches are gaining/losing mass for large/small values of L_i derived from the condition $q_{in} = q_{out}$ (see equations 11, 17, and *SI Appendix*, Fig. S7). When starting from more realistic configurations of patches with a nonzero initial height, $H_i > 0$, the evolution of the bedform presents different phases that are sensitive to the initial mass of sand. For example, when the initial length L_i of the patch is small enough to be in the conditions for which its mass balance is negative, it may not eventually disappear as, while losing mass, it first extends in length and then may reach the other region for which it can begin to gain mass and grow before its height has vanished. Conversely, an initially long patch first increases in height but does so while decreasing in length. If q_{in} is not large enough, the rate of shrinking can outweigh that of growth and the patch eventually disappears. These different examples are displayed in *SI Appendix*, Fig. S7. Importantly, as these analytics are derived for the perfectly flat case, it cannot be used to compare the model to the field data, but allows for a better understanding of the way in which the processes of erosion and deposition work in the model.

Finally we discuss the case for which the input flux is smaller than the transport capacity on the erodible bed: $q_{in} < q^e_{sat}$. For this purpose, it is interesting to consider first steady propagative solutions of the model, computed when imposing $q_{in} = q_{out}$ (both less than q^e_{sat}). Examples of such solutions are discussed in ref. 41 for a single transport law associated with an erodible bed and are displayed in *SI Appendix*, Fig. S8 together with elevation profiles for transport laws that account for both erodible and consolidated beds. Interestingly, when transport capacity is sensitive to the bed nature, but with a vanishing transition length $L_0 = 0$, one obtains identical profiles to the case where the single transport law for an erodible bed is considered, with shapes very close to a symmetric cosine. For those cases, the bedform length is on the order of the cut-off scale of the dune instability $2\pi L_{sat}\mathcal{A}/\mathcal{B}$ (typically $\simeq 10$ m), almost independently of q_{in}. For $L_0 > 0$, the profiles take this characteristic asymmetric, more realistic, shape, and have a smaller length. However, in all cases, the heights are smaller for larger fluxes and vanish when $q_{in} \to q^e_{sat}$. Importantly, these propagative solutions are unstable in the sense that an incoming flux even slightly different to the steady state value makes the bedform evolve away from the steady state solution: If q_{in} is a little too small/large, the bedform shrinks/grows. For initial flat patches, an input flux $q_{in} < q^e_{sat}$ makes bedforms typically shrink and disappear, as illustrated in *SI Appendix*, Fig. S9. Conversely, to make the bedform survive and potentially develop into a dune when $q_{in} < q^e_{sat}$, it must first have sufficiently accumulated sand during the growing phase $q_{in} > q^e_{sat}$ to have reached the critical mass of the steady state solution.

Comparison of the Model to Field Data

The model is able to reproduce the growth and migration of asymmetric sand bedforms similar to those observed in the field that occur when incoming flux is greater than the transport capacity over an erodible bed ($q_{in}/q^e_{sat} \geq 1$). The high-resolution topographic data presented in Fig. 1 provide a comprehensive spatiotemporal coverage of the evolution of such a bedform at the meter scale under a constant wind, which can be used to quantitatively test the theoretical predictions. As the model is two-dimensional, bedform height, length, and position are computed over time from the elevation profiles along a central longitudinal transect (white dashed lines in Fig. 1*B*).

All the results of the theoretical analysis are given with lengths in units of L_{sat} and times in units of L^2_{sat}/Q. For the comparison with the data (Fig. 1), we need to express these length and time scales for the specific values in the field where the measurements have been performed. We take a grain size $d = 255$ µm, densities for the sediment $\rho_{sed} = 2.65 \times 10^3$ kg m^{-3} and the air $\rho_{air} = 1.2$ kg m^{-3}, the bed hydrodynamic roughness $z_0 = 10^{-3}$ m and the gravitational acceleration $g = 9.81$ m s^{-2}. We assume that the saturation length is well estimated by $L_{sat} = 2.2\, d \rho_{sed}/\rho_{air} = 1.24$ m (55), and the threshold shear velocity by $u_{th} = 0.082\sqrt{gd\rho_{sed}/\rho_{air}} \simeq 0.19$ m s^{-1} (1). For the wind velocity measured during the bedform evolution (Fig. 1*C*), this corresponds to a velocity ratio $u_*/u_{th} = 2.8$, or $\tau/\tau_{th} = 7.84$ in terms of shear stress. Similarly, the sand flux constant $Q = 8.3\frac{\rho_{air}u^3_{th}}{\rho_{sed}g} \simeq 2.6 \times 10^{-6}$ m^2 s^{-1} (1), which combined with the saturation length gives the characteristic time scale $L^2_{sat}/Q = 5.9 \times 10^5$ s $\simeq 7$ d. Finally, with the two transport laws [**4** and **5**], we obtain saturated sand fluxes over erodible $q^e_{sat} \simeq 1.8 \times 10^{-5}$ m^2 s^{-1} and consolidated $q^c_{sat} \simeq 5.0 \times 10^{-5}$ m^2 s^{-1} beds.

The primary parameters of the model that require adjustment to fit the field data are the incoming sand flux q_{in} and the transition length L_0. Starting the simulation with a given almost

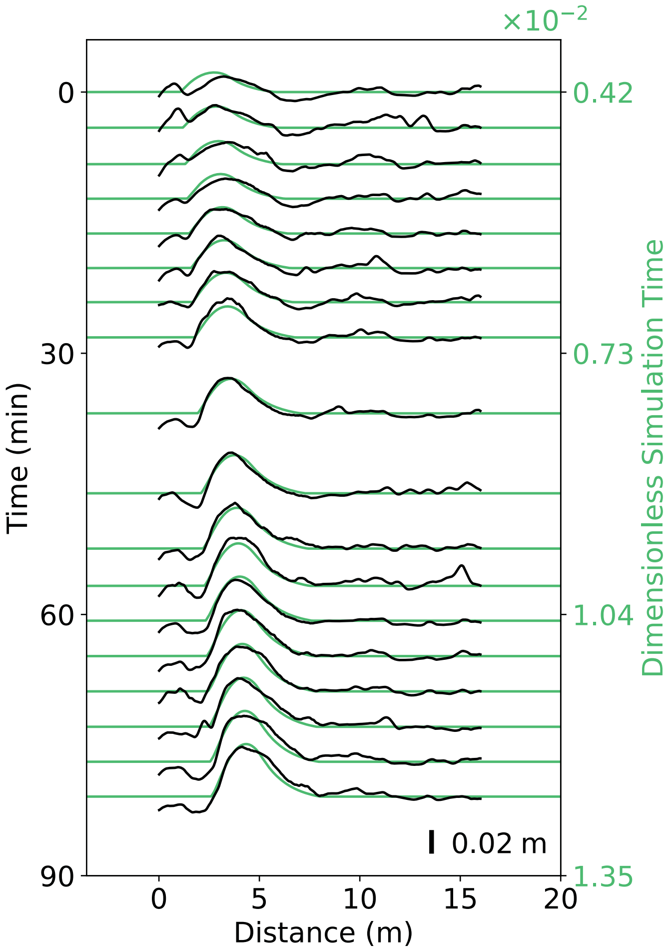

Fig. 4. Model adjustment to field data. Black lines: spatiotemporal diagram with the elevation profiles of the central transect of the meter-scale bedform shown in Fig. 1*B*. Green lines: profiles from the model when the parameters are adjusted to the values $\{L_0/L_{sat}, q_{in}/q_{sat}^{e}\} = \{2.0, 2.0\}$ that best fit the time evolution of bedform height, position, and length (Fig. 1*C*). Time origin is 9:40 am. The ensemble of parameter values giving a reasonable fit of the data is displayed in Fig. 3 as a red ellipse. *Right* axis in green: dimensionless time in the simulation.

flat patch, q_{in} and L_0 are tuned to reproduce the time evolution of the bedform height, length, and displacement (green lines in Fig. 1*C*). This tuning results in full elevation profiles that are remarkably well-adjusted, with a quantitative capture of the shape, growth, and migration of the sand deposit over time (Fig. 4). In fact, it is also necessary to adjust two other quantities, the time and space at which the comparison to the measured profiles begins. However, these are inconsequential offsets, essentially associated with the arbitrary choice of the initial patch height and length at time $t = 0$. They do not affect the optimum q_{in} and L_0 to fit the data (*SI Appendix*, Figs. S10 and S11). The values of these two parameters are also robust with respect to the criterion used to distinguish consolidated and erodible beds (the value of h_s), as well as the choice for the transition profile of the transport capacity (Eq. **6**). Furthermore, it was verified that the numerical integration steps do not influence the results as soon as they are sufficiently small ($dt \leq 10^{-6}$ with $dx = 10^{-3}$).

Accounting for these various sources of uncertainty, the fitting process of the dataset displayed in Fig. 1 gives $q_{in}/q_{sat}^{e} \simeq 2.0$ and $L_0/L_{sat} \simeq 2.0$, with error bars on the order of 25%. These ranges of values are represented in Fig. 3 by ellipses centered on the main values. As expected, they belong to the region of the parameter space associated with the growth and migration of bedforms. The same analysis performed on another bedform that emerged 30 min later in the same area and under the same wind conditions gives consistent predictions (see second ellipse in Fig. 3 and elevation profiles in *SI Appendix*, Fig. S12).

We have also run the model to reproduce the dynamics of a shrinking bedform similar to that of Fig. 1*B*, after the wind has started to change direction and reduce strength, yet still above transport threshold. The data show the evolution of elevation profiles that keep similar asymmetric shapes, but whose height and length decrease in time (*SI Appendix*, Fig. S13). We have accounted for the fact that the wind reduces with time, inducing a decreasing q_{sat}^{e}. The data can be fitted with an input flux proportional but significantly smaller than q_{sat}^{e} and, perhaps more surprisingly, with a vanishing L_0. One can speculate on the relevance of any transition distance at low transport, but this case clearly requires more investigation.

Finally, *SI Appendix*, Fig. S16 provides field evidence of the third spreading regime, where we observed sand accumulation at the upwind side of the bedform over a period of approximately 2 h (64). However, these data are too sparse to be used for model parameter fitting.

Discussion and Perspectives

The quantitative agreement between the theoretical predictions of the present model and the field measurements provides compelling evidence to explain the growth and migration of meter-scale bedforms, i.e. that are smaller than the minimum dune size predicted by linear stability analysis of a flat sand bed (12, 41, 49). Our analysis shows how the dynamics of these bedforms is governed by bed heterogeneities, which modify the aeolian transport capacity when the nature of the bed, whether erodible or consolidated, changes. The typical asymmetrical shape of the observed elevation profiles is representative of an overall depositional process, resulting from a strong incoming flux that is oversaturated for saltation on a sandy bed (14, 33). At the same time, erosion also occurs at the upwind edge of the bedforms, which induces their migration. This requires a local increase in sand flux, which is only possible if the transport capacity does not drop sharply, but over some specific distance, when the bed transitions from a consolidated to an erodible configuration.

Given the necessity of having a large incoming flux $q_{in} > q_{sat}^{e}$ to observe the growth of these meter-scale sand bedforms, one must first ask where all this sand is coming from. On beaches or in the presence of wet sand beds, one can argue that surface grains can dry out or be mobilized by impacts to erode, and gradually increase transport (65, 66). In arid desert dune fields however, where the consolidated bed in the interdune is mainly composed of coarse-grains or gravels, the output flux from a dune can hardly exceed the value of q_{sat}^{e}. In this case, the saltation flux must gradually increase as it travels over interdune areas, mobilizing the sand grains trapped between the larger particles by impacts or wind shear stress. An alternative explanation is to consider ephemeral sand deposits from saltation streamers, which could provide a significant amount of sand for transport when they disappear. The dynamics of saltation flux in the interdune areas or on the beaches could then be more dynamic than expected and a key process in the life of small-scale bedforms. This certainly merits further field studies measuring the input and output fluxes of these bedforms. In this perspective, the model proposed herein provides theoretical predictions of the magnitude of these fluxes as a function of the observed dynamics. In places where field measurements are not possible, this approach provides a means of using small-scale aeolian bedforms, evolving on short timescales, to provide valuable constraints on atmospheric flows and the associated sand fluxes.

In terms of the physics of sediment transport, an essential component of the present model is the transition length, L_0, which governs the change in transport capacity when bed properties change from a consolidated state to an erodible state, or vice versa. One would like to gain understanding of the physical processes at work in this transition. Valid questions might include whether these physical processes could be interpreted in terms of grain rebounds (33, 63), or associated with the saturation length, or whether there is a dependence of L_0 on wind velocity. Of course, the saturated flux q_{sat} that quantifies this transport capacity cannot be measured directly and, while we are able to measure the actual flux, it is very challenging to obtain complete flux profiles $q(x)$ over various heterogeneous beds. At a microscopic level, recording the trajectories of saltating grains along the transition between the two types of bed are also desirable data that could be collected in the field as well as in wind tunnels. Theoretical analysis of such profiles and trajectories would be a useful way to improve current understanding of the transport processes associated with this transition, and how they relate to L_0.

The predicted bedforms do not reach a steady state, but instead exhibit three transient dynamics: increasing in height while migrating, disappearing, or growing in place while spreading. They must continue to be documented in the field in order to provide a more comprehensive picture of their out-of-equilibrium behavior. Further high-precision spatiotemporal data similar to those acquired in the Namib Desert should be obtained, particularly for bedforms in the disappearing and spreading regimes, as well as for various wind/grain/surface conditions. Another interest is to follow the dynamics of these bedforms over longer times, ideally over their entire life. The aim is then to identify the conditions under which they could become large enough to transform into dunes (2), for example on moist surfaces of beaches (67–69). By combining numerical predictions and observations, the first step will be to estimate the strength and duration of the wind events that generate the appropriate incoming flux conditions to reach the spreading regime. As the model predicts bedform disappearance when $q_{\mathrm{in}}/q_{\mathrm{sat}}^{\mathrm{e}} \leq 1.2$ (Fig. 3 for L_0/L_{sat} between 1 and 3), all these studies will also help to quantify the ephemeral existence of meter-scale sand deposits, and link their occurrence to specific atmospheric episodes. Also, in addition to their small size, it is worth considering whether a new branch should be added to the classification of aeolian dunes (1) for such transient or ephemeral bedforms.

At the larger length scale of a population of these bedforms (Fig. 1 *A*, *Top*), the study of their interactions, mediated by the sand flux, and possibly their resulting spatial organization, as illustrated in refs. 67–69 on a beach environment, is of primary interest. A deeper understanding of their collective dynamics would allow them to be better identified, observed, and tracked in the field and on aerial imagery. As they can disappear rapidly in weak or multidirectional wind conditions, their occurrence and resilience to different wind regimes would provide essential indirect information on sediment transport in areas of limited sand availability.

Finally, our work also suggests the need to investigate the complementary configuration, where a delimited area of consolidated surface is present in the middle of a mostly erodible bed. This has been observed, for example, on the dunes of the White Sands (New Mexico, USA), where when sufficiently humid, the gypsum grains stick to each other, providing such a consolidated surface over which mobile grains can be transported by the wind. How can such "holes" of mobile grains develop and possibly move? Precise spatiotemporal data are needed to test these new ideas.

Materials and Methods

We provide here details on how the equations of the model are numerically integrated, and in particular how bed elevation h and sand flux q are incremented over time, especially when erosion/deposition is limited by the consolidated bed.

Starting from given initial conditions, one first computes at each time step the along wind x-profiles of:

- The basal shear stress with $\tau(x,t) = \tau_0 \left[1 + \mathcal{A}\,\mathrm{IFFT}(k\hat{h}) + \mathcal{B}\,\partial_x h\right]$, where τ_0 is its reference value in the base (flat) state. Following notations of the main text, $\hat{h}(k)$ is the (fast) Fourier transform (FFT) of $h(x)$, and IFFT denotes the inverse transformation. $\mathcal{A}$ and $\mathcal{B}$ are constants here set to 3 and 1.5 respectively (12).
- The saturated flux $q_{\mathrm{sat}}(x,t)$ from the transport laws with the above profile of τ, accounting for the nature of the bed (erodible vs. consolidated; see Eqs. **4** and **5**) as well as for the transition region at the switch from two bed states (Eq. **6**). Importantly, the saturated flux must not be negative, and if this calculation gives $q_{\mathrm{sat}} < 0$ in some space intervals, we instead set it to 0 there. In practice, this only happens at very late states of the bedform evolution, when the bed elevation profile becomes very steep and for which other aspects of the model should be modified [e.g., introduction of a recirculation bubble (41)]. None of the present results have reached this point.

The flux is then deduced from the relaxation equation (Eq. **2**), here integrated through an explicit first-order scheme in space:

$$q(x,t) = \frac{q(x-\mathrm{d}x,t) + \frac{\mathrm{d}x}{L_{\mathrm{sat}}}\, q_{\mathrm{sat}}(x,t)}{1 + \frac{\mathrm{d}x}{L_{\mathrm{sat}}}} \qquad \textbf{[7]}$$

starting from $q = q_{\mathrm{in}}$ at the up-wind side of the integration domain. Simultaneously, the bed elevation profile is up-dated with an explicit first-order scheme in time:

$$h(x,t+\mathrm{d}t) = h(x,t) - \frac{\mathrm{d}t}{L_{\mathrm{sat}}}\,\left(q_{\mathrm{sat}}(x,t) - q(x,t)\right) \qquad \textbf{[8]}$$

At each grid point, we check that one does not erode more sand than available, and if the above calculation gives $h(x,t+\mathrm{d}t) < 0$, we set $h(x,t+\mathrm{d}t) = 0$ and correct the sand flux as $q(x,t) = q(x-\mathrm{d}x,t) + \frac{\mathrm{d}x}{\mathrm{d}t}\,h(x,t)$, so that mass conservation [**1**] is still satisfied–but [**7**] is not. This applies in particular to the up-wind part of the domain, before the bedform, where the bed is flat with no sand available for erosion ($h = 0$), and where $q = q_{\mathrm{in}} < q_{\mathrm{sat}}^{c}$ must be kept constant.

Data, Materials, and Software Availability. Datasets have been deposited in refs. 42, 43, and 64. The code integrating the equations of the model is available in ref. 70.

ACKNOWLEDGMENTS. We thank B. Andreotti, S. Courrech du Pont, C. Gadal, N. Bristow, and The Origin of Aeolian Dunes project partners for discussions. C.N. acknowledges financial support from the French National Research Agency (ANR-23-CE56-0008/EOLE), the UnivEarthS LabEx program (ANR-10-LABX-0023), and the Initiative d'Excellence Université de Paris (ANR-18-IDEX-0001). Funding for the field component of this research is gratefully acknowledged from Natural Environment Research Council, UK, and NSF, USA (NE/R010196/1 NSFGEO-NERC; NSF-GEO-1829541; and NSF-GEO-1829513). We thank the Gobabeb Namib Research Institute and G. Maggs-Kolling and E. Marais for field support and site identification and S. Nangolo and R. Huck for field assistance. We acknowledge the Namibia Ministryof Environment, Forestry and Tourism, National Commission on Research, Science and Technology, Namibia, and Namib-Naukluft National Park (permit RPIV00052018). Field data processing used the Iridis Southampton Computing Facility. Thanks to P. Morgan and the Southampton Geography and Environmental Science Technician Team for undertaking the grain size analysis. We are grateful for Great Sand Dunes National Park and Preserve fieldwork assistance from A. Valdez and F. Bunch (permit GRSA-2018-SCI-004). For the purpose of open access, the author has applied a Creative Commons Attribution (CC BY) license to any Author Accepted Manuscript version arising. We thank the referees and the editor for constructive reviews.

Author affiliations: [a]Physique et Mécanique des Milieux Hétérogènes, CNRS, Ecole Supérieure de Physique de de Chimie Industrielles de la ville de Paris, Paris Sciences & Lettres Research University, Université Paris Cité, Sorbonne Université, Paris 75005, France; [b]School of Geography and Environmental Science, University of Southampton, Southampton SO17 1BJ, United Kingdom; [c]Université Paris Cité, Institut de physique du Globe de Paris, CNRS, Paris 75005, France; [d]Laboratoire de Géologie, Ecole Normale Supérieure, CNRS, Paris Sciences & Lettres Research University, Paris 75005, France; [e]School of Geography and the Environment, University of Oxford, Oxford OX1 3QY, United Kingdom; [f]Department of Geography and Environment, Loughborough University, Loughborough LE11 3TU, United Kingdom; [g]Departments of Earth Science and Environmental Change, Geography and Geographic Information Science, and Mechanical Science and Engineering, and Ven Te Chow Hydrosystems Laboratory, University of Illinois at Urbana-Champaign, Urbana, IL 61801; and [h]Department of Mechanical Engineering, University of Colorado Denver, Denver, CO 80204

1. S. Courrech *et al*., Complementary classifications of aeolian dunes based on morphology, dynamics, and fluid mechanics. *Earth Sci. Rev.* **255**, 104772 (2024).
2. G. Kocurek, M. Townsley, E. Yeh, K. Havholm, M. Sweet, Dune and dune-field development on Padre Island, Texas, with implications for interdune deposition and water-table-controlled accumulation. *J. Sediment. Res.* **62**, 622–635 (1992).
3. A. L. Montreuil *et al*., Early-stage aeolian dune development and dynamics on the upper-beach. *J. Coast. Res.* **95**, 336–340 (2020).
4. N. Lancaster, Field studies of sand patch initiation processes on the northern margin of the Namib Sand Sea. *Earth Surf. Process. Landf.* **21**, 947–954 (1996).
5. P. A. Hesp, S. M. Arens, Crescentic dunes at Schiermonnikoog, the Netherlands. *Earth Surf. Process. Landf.* **22**, 785–788 (1997).
6. H. Elbelrhiti, P. Claudin, B. Andreotti, Field evidence for surface-wave-induced instability of sand dunes. *Nature* **437**, 720–723 (2005).
7. J. M. Nield, G. F. S. Wiggs, R. S. Squirrell, Aeolian sand strip mobility and protodune development on a drying beach: examining surface moisture and surface roughness patterns measured by terrestrial laser scanning. *Earth Surf. Process. Landf.* **36**, 513–522 (2011).
8. H. Elbelrhiti, Initiation and early development of barchan dunes: A case study of the Moroccan Atlantic Sahara desert. *Geomorphology* **138**, 181–188 (2012).
9. N. R. Bristow *et al*., Topographic perturbation of turbulent boundary layers by low-angle, early-stage aeolian dunes. *Earth Surf. Process. Landf.* **47**, 1439–1454 (2022).
10. C. Gadal *et al*., Spatial and temporal development of incipient dunes. *Geophys. Res. Lett.* **47**, e2020GL088919 (2020).
11. P. Delorme *et al*., Dune initiation in a bimodal wind regime. *J. Geophys. Res.* **125**, e2020JF005757 (2020).
12. P. Lü *et al*., Direct validation of dune instability theory. *Proc. Natl. Acad. Sci. U.S.A.* **118**, e2024105118 (2021).
13. M. Baddock, J. Nield, G. Wiggs, Early-stage aeolian protodunes: Bedform development and sand transport dynamics. *Earth Surf. Process. Landf.* **43**, 339–346 (2018).
14. P. Delorme *et al*., Field evidence for the initiation of isolated aeolian sand patches. *Geophys. Res. Lett.* **50**, e2022GL101553 (2023).
15. R. Anderson, A theoretical model for aeolian impact ripples. *Sedimentology* **34**, 943–956 (1987).
16. Z. Csahók, C. Misbah, F. Rioual, A. Valance, A theoretical model for aeolian impact ripples. *Eur. Phys. J. E* **3**, 71–86 (2000).
17. H. Yizhaq, N. Balmforth, A. Provenzale, Blown by wind: Nonlinear dynamics of aeolian sand ripples. *Phys. D* **195**, 207–228 (2004).
18. O. Duran, P. Claudin, B. Andreotti, Direct numerical simulations of aeolian sand ripples. *Proc. Natl. Acad. Sci. U.S.A.* **111**, 15665–15668 (2014).
19. C. W. Lester, A. B. Murray, O. Durán Vinent, B. Andreotti, P. Claudin, Emergence of wind ripples controlled by mechanics of grain-bed impacts. *Nat. Geosci.* **18**, 344–350 (2025).
20. R. A. Bagnold, The transport of sand by wind. *Geogr. J.* **89**, 409–438 (1937).
21. R. A. Bagnold, *The Physics of Wind Blown Sand and Desert Dunes* (Methuen, London, 1941), vol. 265.
22. P. Nalpanis, J. Hunt, C. Barrett, Saltating particles over flat beds. *J. Fluid Mech.* **251**, 661–685 (1993).
23. K. R. Rasmussen, J. D. Iversen, P. Rautaheimo, Saltation and wind flow interaction in a variable slope wind tunnel. *Geomorphology* **17**, 19–28 (1996).
24. J. Iversen, K. Rasmussen, The effect of wind speed and bed slope on sand transport. *Sedimentology* **46**, 723–731 (1999).
25. Z. Dong, X. Liu, X. Wang, F. Li, A. Zhao, Experimental investigation of the velocity of a sand cloud blowing over a sandy surface. *Earth Surf. Process. Landf.* **29**, 343–358 (2004).
26. K. Rasmussen, M. Sorensen, Vertical variation of particle speed and flux density in aeolian saltation: Measurement and modeling. *J. Geophys. Res.* **113**, F02S12 (2008).
27. M. Creyssels *et al*., Saltating particles in a turbulent boundary layer: Experiment and theory. *J. Fluid Mech.* **625**, 47–74 (2009).
28. T. D. Ho, P. Dupont, A. Ould El Moctar, A. Valance, Particle velocity distribution in saltation transport. *Phys. Rev. E* **85**, 052301 (2012).
29. T. D. Ho, A. Valance, P. Dupont, A. O. El Moctar, Aeolian sand transport: Length and height distributions of saltation trajectories. *Aeolian Res.* **12**, 65–74 (2014).
30. R. L. Martin, J. F. Kok, Wind-invariant saltation heights imply linear scaling of aeolian saltation flux with shear stress. *Sci. Adv.* **3**, e1602569 (2017).
31. A. Valance, K. R. Rasmussen, A. O. El Moctar, P. Dupont, The physics of aeolian sand transport. *C. R. Phys.* **16**, 105–117 (2015).
32. T. Pähtz, O. Durán, Unification of aeolian and fluvial sediment transport rate from granular physics. *Phys. Rev. Lett.* **124**, 168001 (2020a).
33. T. Ho, A. Valance, P. Dupont, A. Ould El Moctar, Scaling laws in aeolian sand transport. *Phys. Rev. Lett.* **106**, 094501 (2011).
34. J. M. Nield, G. F. S. Wiggs, The application of terrestrial laser scanning to aeolian saltation cloud measurement and its response to changing surface moisture. *Earth Surf. Process. Landf.* **36**, 273–278 (2011).
35. P. O'Brien, C McKenna Neuman, Effect of the surface water content on dry saltation cloud dynamics: A wind tunnel simulation with particle tracking velocimetry. *Earth Surf. Process. Landf.* **48**, 3103–3114 (2023).
36. O. Durán, P. Claudin, B. Andreotti, On aeolian transport: Grain-scale interactions, dynamical mechanisms and scaling laws. *Aeol. Res.* **3**, 243–270 (2011).
37. O. Durán, B. Andreotti, P. Claudin, Numerical simulation of turbulent sediment transport, from bed load to saltation. *Phys. Fluids* **24**, 103306 (2012).
38. J. Jenkins, A. Valance, Periodic trajectories in aeolian sand transport. *Phys. Fluids* **26**, 073301 (2014).
39. D. Berzi, J. Jenkins, A. Valance, Periodic saltation over hydrodynamically rough beds: Aeolian to aquatic. *J. Fluids Mech.* **786**, 190–209 (2014).
40. J. Nield, Surface moisture-induced feedback in aeolian environments. *Geology* **39**, 915–918 (2011).
41. B. Andreotti, P. Claudin, S. Douady, Selection of dune shapes and velocities: Part 2: A two-dimensional modelling. *Eur. Phys. J. B* **28**, 341–352 (2002).
42. J. Nield, M. Baddock, G. Wiggs, Surface and Meteorological Data of Protodune Dynamics at Helga's Interdune Area, Gobabeb, Namib Desert, Namibia on 13th September 2022. (Dataset). NERC EDS National Geoscience Data Centre. https://doi.org/10.5285/10203f53-7471-4b8e-8177-74aef66bb432. Deposited Deposited 10 October 2023.
43. J. Nield *et al*., Surface and Meteorological Data of Protodune Dynamics at Helga's Interdune Area, Gobabeb, Namib Desert, Namibia on 12th September 2023. (Dataset). NERC EDS National Geoscience Data Centre. https://doi.org/10.5285/786969f7-ff58-42d3-9175-3f792a7fd9f7. Deposited Deposited 27 February 2025.
44. K. Kroy, S. Sauermann, H. Herrmann, Minimal model for sand dunes. *Phys. Rev. Lett.* **88**, 054301 (2002).
45. K. Kroy, S. Sauermann, H. Herrmann, Minimal model for aeolian sand dunes. *Phys. Rev. E* **66**, 031302 (2002).
46. P. Hersen *et al*., Corridors of barchan dunes: Stability and size selection. *Phys. Rev. E* **69**, 011304 (2004).
47. P. Hersen, On the crescentic shape of barchan dunes. *Eur. Phys. J. B* **37**, 507–514 (2004).
48. O. Durán, E. J. R. Parteli, H. J. Herrmann, A continuous model for sand dunes: Review, new developments and application to barchan dunes and barchan dune fields. *Earth Surf. Process. Landf.* **35**, 1591–1600 (2010).
49. F. Charru, B. Andreotti, P. Claudin, Sand ripples and dunes. *Annu. Rev. Fluid Mech.* **45**, 469–493 (2013).
50. S. Courrech du Pont, Dune morphodynamics. *C. R. Phys.* **16**, 118–138 (2015).
51. C. M. Neuman, M. M. Scott, A wind tunnel study of the influence of pore water on aeolian sediment transport. *J. Arid Environ.* **39**, 403–419 (1998).
52. F. M. Exner, *Zur physik der dünen* (Hölder, 1920).
53. F. M. Exner, Uber die wechselwirkung zwischen wasser und geschiebe in flusen. *Sitz-Ber. Akad. Wiss. Wien* **1**, 1 (1925).
54. G. Sauermann, K. Kroy, H. J. Herrmann, Continuum saltation model for sand dunes. *Phys. Rev. E* **64**, 031305 (2001).
55. B. Andreotti, P. Claudin, O. Pouliquen, Measurements of the aeolian sand transport saturation length. *Geomorphology* **123**, 343–348 (2010).
56. T. Pähtz, O. Durán, Fluid forces or impacts: What governs the entrainment of soil particles in sediment transport mediated by a Newtonian fluid? *Phys. Rev. Fluids* **2**, 074303 (2017).
57. M. Lämmel, K. Kroy, Analytical mesoscale modeling of aeolian sand transport. *Phys. Rev. E* **96**, 052906 (2017).
58. H. Selmani, A. Valance, A. Ould El Moctar, P. Dupont, R. Zegadi, Aeolian sand transport in out-of-equilibrium regimes. *Geophys. Res. Lett.* **45**, 1838–1844 (2018).
59. P. Claudin, G. F. S. Wiggs, B. Andreotti, Field evidence for the upwind velocity shift at the crest of low dunes. *Bound. Layer Meteorol.* **148**, 195–206 (2013).
60. J. E. Ungar, P. K. Haff, Steady state saltation in air. *Sedimentology* **34**, 289–299 (1987).
61. B. Andreotti, A two-species model of aeolian sand transport. *J. Fluid Mech.* **510**, 47–70 (2004).
62. J. L. Ralaiarisoa *et al*., Transition from saltation to collisional regime in windblown sand. *Phys. Rev. Lett.* **124**, 198501 (2020).
63. S. Kamath, Y. Shao, E. J. R. Parteli, Scaling laws in aeolian sand transport under low sand availability. *Geophys. Res. Lett.* **49**, e2022GL097767 (2022).
64. J. Nield, M. Baddock, G. Wiggs, Surface and Meteorological Data of Protodune Dynamics at Medano Creek Area, Great Sand Dunes National Park, Colorado, USA on 3rd April 2023. (Dataset). NERC EDS National Geoscience Data Centre. https://doi.org/10.5285/95fb2393-954a-4217-86aa-cb10fb3996c5. Deposited Deposited 27 February 2025.

65. Cooper Jackson, Beach fetch distance and aeolian sediment transport. *Sedimentology* **46**, 517–522 (1999).
66. G. Strypsteen, I. Delgado-Fernandez, J. Derijckere, P. Rauwoens, Fetch-driven aeolian sediment transport on a sandy beach: A new study. *Earth Surf. Process. Landf.* **49**, 1530–1543 (2024).
67. P. Hage, G. Ruessink, J. Donker, Determining sand strip characteristics using Argus video monitoring. *Aeolian Res.* **33**, 1–11 (2018).
68. P. Hage, G. Ruessink, Z. van Aartrijk, J. Donker, Using video monitoring to test a fetch-based aeolian sand transport model. *J. Mar. Sci. Eng.* **8**, 110 (2020).
69. C. van IJzendoorn *et al*., Detection and characterization of aeolian sand strips on the beach using permanent laser scanning. *Geomorphica* **1**, 1–21 (2024).
70. C. Rambert, C. Narteau, P. Claudin, Python code used to compute bedform profiles. IPGP. https://www.ipgp.fr/~narteau/PATCH/. Deposited 12 April 2025.